ORIGINAL PAPER

Chevkinite-group minerals in selected intrusions of the Mazury Complex, North-Eastern Poland: insights into the formation of a titanite-like phase by hydrothermal alteration

Justyna Domańska-Siuda[1] · Krzysztof Nejbert[1] · Bogusław Bagiński[1] · Ray Macdonald[1,2] · Jakub Kotowski[1] · Marcin Stachowicz[1]

Abstract

Chevkinite-group minerals forming large and common (up to 0.03 vol%) accessory phases in monzodiorites and granodiorites from the Mesoproterozoic anorthosite-mangerite-charnockite-granite (AMCG) suite intrusions, Mazury Complex, north-eastern Poland, range from pristine magmatic types to hydrothermally altered varieties. The unaltered phase is perrierite-(Ce), with the uncommon feature of having Al dominant in the C site. Hydrothermal alteration of the perrierite-(Ce) followed two main trends: one shows depletion in Ca, Fe, Si, Al and Mg, and increasing Ti contents; the other shows increases in Si, Ti and Ca and decreases in light rare-earth elements (LREE), Y and Mg, at about constant Fe content. The second trend resulted in the formation of a phase compositionally similar to titanite. Result of chemical analyses show that the transition from perrierite-(Ce) to the titanite-like phase is sharp; an electron back-scatter diffraction (EBSD) study shows the titanite-like material to be amorphous. The hydrothermal alteration of a chevkinite-group mineral to titanite has commonly been reported in natural sequences but this is the first record of the identification of a titanite-like phase made on the basis of a structural analysis.

Introduction

The chevkinite-group minerals (CGM) are increasingly being recognized as important accessory phases in a wide range of igneous and metamorphic rocks. They are known from hundreds of localities and undoubtedly occur unreported in hundreds more (Macdonald et al. 2019). The group comprises twelve members, the generally accepted formula being $A_4BC_2D_2(Si_2O_7)_2O_8$, where $A = REE$, Ca, Sr, Th; $B = Fe^{2+}$; $C = Fe^{2+}$, Fe^{3+}, Ti, Al; $D = Ti$. However, varieties rich in Zr, Nb, Mn and W are also known. During our ongoing studies of Mesoproterozoic intrusions in NE Poland, we have found CGM which are of particular interest. First, the minerals are unusually large and common and are also texturally very variable. Second, they show the uncommon feature of Al dominance in the C site.

Like other REE-bearing accessory minerals, CGM are prone to alteration by hydrothermal fluids. There is a wide range of alteration mechanisms and products, mainly related to the nature of the ligands in the fluids, as reviewed by Macdonald et al. (2019). In the Mazury rocks, we report two modes of hydrothermal alteration, one of them representing an intermediate stage in the breakdown of a CGM to a titanite-like phase, which has been amenable to investigation by electron probe microanalysis (EPMA) and electron back-scattered diffraction (EBSD).

✉ Justyna Domańska-Siuda
j.domanska@uw.edu.pl

1 Faculty of Geology, Department of Geochemistry, Mineralogy and Petrology, University of Warsaw, ul. Żwirki i Wigury 93, 02-089 Warsaw, Poland

2 Environment Centre, Lancaster University, Lancaster LA1 4YQ, UK

Geological setting

The rocks studied here have been sampled from three boreholes, Krasnopol PIG-6, Pawłówka PIG-1A, and Filipów IG-1 (Fig. 1) located in the crystalline basement of northeastern Poland. The intrusion are built of rapakivi-type granitoids (sensu Haapala et al. 2005) that is are the A-type granites of large batholiths, which include varieties with the rapakivi texture (sensu Vorma 1976; Happala and Rämö 1992; Rämö and Haapala 1995) and associated intermediate and mafic rocks. It belongs to a widespread set of rapakivi-type granitoid intrusions in northern Poland, which together with anorthositic massifs (Suwałki, Sejny and Kętrzyn) form the so-called Mazury Complex (Kubicki and Ryka 1982, 1993). The complex forms a belt of granitoid and associated mafic (anorthositic) and intermediate bodies intruded within the older metamorphic basement of the Eastern European platform and extends over 300 km from the Baltic Sea (near Elbląg in northern Poland) to the Kabeliai and Veisiejai complexes in eastern Lithuania (Skridlaite et al. 2003). The boundaries between individual intrusions in the Mazury Complex in Poland are poorly defined because their structure is based mainly on a few boreholes and geophysical data (Ryka and Sawicki 1980; Kubicki and Ryka 1982; Wybraniec 1999).

Granitoid intrusions of the Mazury Complex are examples of a widespread series of rapakivi granitoids (Happala

and Rämö 1992; Rämö and Haapala 1995; Bagiński et al. 2001; Duchesne et al. 2010). These intrusions form massifs of varying sizes, often occurring with anorthosite intrusions, both with features typical of anorogenic magmatism. The crystallization ages of the rapakivi intrusions are in the range 1.81 – 1.47 Ga (Happala and Rämö 1992, 1999; Rämö and Haapala 1995; Shumlyanskyy et al. 2017). The crystallization ages of rapakivi granitoids from the Mazury Complex range from 1548 to 1499 Ma, some 50 Ma (Dorr et al. 2002; Wiszniewska et al. 2007). Two samples of quartz monzonite from the Gołdap and Bartoszyce boreholes yielded U–Pb zircon ages of 1502 ± 2 Ma and 1499 ± 4 Ma, respectively (Claesson et al. 1995). The crystallization age of the rapakivi granitoids at Filipów (Fig. 1) is estimated at 1512 ± 17 Ma based on results of U-Th-Pb zircon SIMS (secondary ion mass spectrometry) analyses (Wiszniewska et al. 2016). The crystallization ages of granites from the Kabeliai and Veisiejai intrusions (in eastern Lithuania) fit the age range of the Mazury Complex, e.g. the 1505 Ma age of the Kabeliai granites in southeastern Lithuania (Sundblad et al. 1994).

The samples studied here come from different depths of the Krasnopol PIG-6, Pawłówka PIG-1A, and Filipów IG-1 boreholes, as listed in Table 1. Compositionally, the rocks straddle the boundary between monzonite and diorite and SiO2 contents range from ~ 56 to 65 wt%. Bagiński et al. (2001), Dörr et al. (2002) and Duchesne et al. (2010) noted that the rocks are metaluminous, with geochemical affinities to A-type suites.

Fig. 1 Geological sketch of the north-eastern part of the crystalline basement in NE Poland (modified after Kubicki and Ryka 1982; Ryka 1982, 1993)
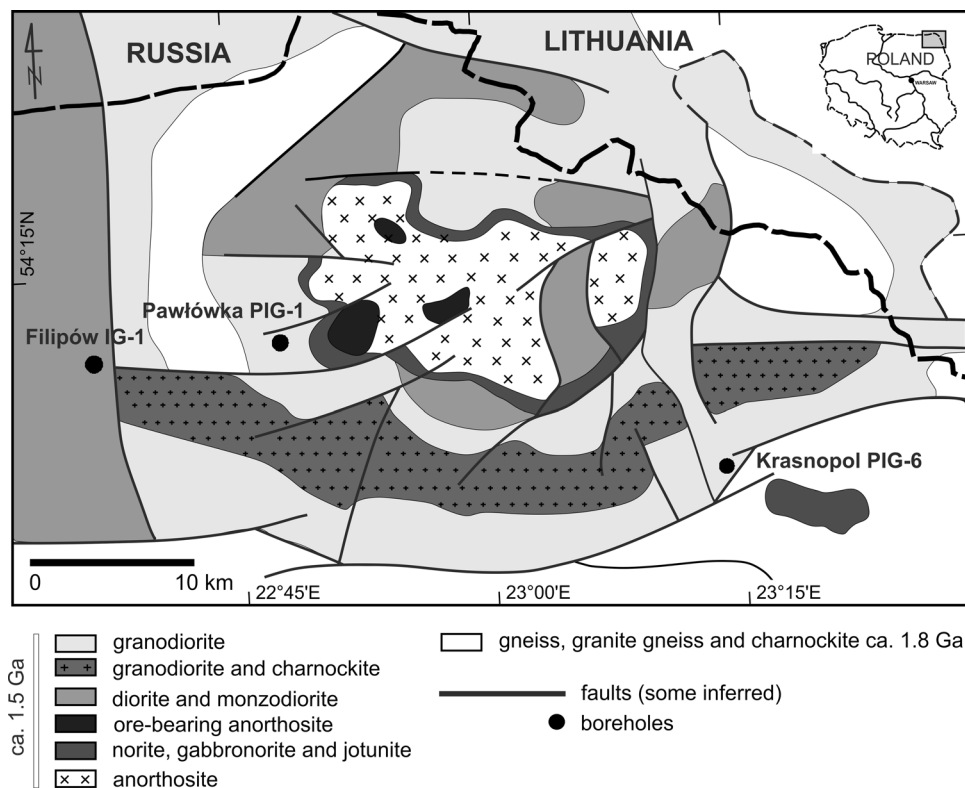
Table 1 Occurrences of chevkinite-group minerals (CGM)

Sample	Sample description	CGM Texture
Kr-6–2 the Krasnopol PIG-6 drillhore	Light pink granodiorite, coarse-grained. The size of plagioclase phenocrysts in the sample reaches up to 4 cm	large euhedral grains and regularly distributed lamellar inclusion in plagioclase phenocrysts
Kr-6–19 the Krasnopol PIG-6 drillhore	Light pink granodiorite, coarse-grained. The size of plagioclase phenocrysts in the sample reaches up to 3 cm	large euhedral, subhedral or anhedral grains and regularly distributed lamellar inclusions in plagioclase phenocrysts and biotite
Kr-6–33 the Krasnopol PIG-6 drillhore	Light grey granodiorite, coarse-grained. The size of plagioclase phenocrysts in the sample reaches up to 4 cm	large euhedral, subhedral or anhedral grains
Kr-6–37 the Krasnopol PIG-6 drillhore	A non-oriented fine-grained enclave, monzodiorite in composition, within coarse-grained granodiorite with a porphyritic texture host. The enclave contains plagioclase megacrysts up to 0.5 cm. There are a lot of fine Fe-Ti oxides in the enclave	large euhedral grains and regularly distributed lamellar inclusions in plagioclase megacrysts
Kr-6–41 the Krasnopol PIG-6 drillhore	A non-oriented fine-grained enclave, monzodiorite in composition, within coarse-grained granodiorite with a porphyritic texture host	large euhedral, subhedral or anhedral grains
Kr-6–59 the Krasnopol PIG-6 drillhore	Partly diffuse contact of the non-oriented, fine-grained monzodiorite enclave with the porphyritic, coarse-grained granodiorite. Large feldspar megacrysts cross the contacts between enclave and granodiorite. The size of plagioclase megacrysts in the sample reaches up to 1.5 cm	large euhedral, subhedral or anhedral grains
Filipów-1 the Filipów IG-1 drillhore	Medium-grained, even-grained granodiorite, plagioclase phenocrysts up to 1 cm in size. Macroscopic visible Fe-Ti oxides and sulfides that coexist with biotite and amphibole	large euhedral grains and regularly distributed lamellar inclusions in plagioclase phenocrysts
Pa-2–28 the Pawłówka PIG-1A drillcore	Light grey granodiorite, coarse-grained. The size of plagioclase phenocrysts in the sample reaches up to 2.5 cm	regularly distributed lamellar inclusions in plagioclase phenocrysts
Pa-2–40 the Pawłówka PIG-1A drillcore	Gray-red granodiorite, coarse-grained	regularly distributed lamellar inclusions in biotite

The A/CNK indices [aluminium saturation index: molar ratio of $Al_2O_3/(CaO + Na_2O + K_2O)$] from Pawłówka PIG-1A and Filipów IG-1 are 0.84 – 0.95 and 0.82 – 0.93, respectively (Bagiński et al. 2001). The rocks from Krasnopol PIG-6 are more diverse, with A/CNK in the range 0.66 – 0.93 (Dörr et al. 2002, and our unpublished data). The Mg-numbers [atomic ratio of $100 \times (Mg/(Mg + Fe))$] are similar and vary in the following ranges: 33 – 35 for Filipów IG-1, 31 – 32 for Pawłówka PIG-1A and 28 – 33 for Krasnopol PIG-6. The Na_2O/K_2O ratios are < 1 and the rocks plot in the high-K field of the Rickwood (1989) diagram (not shown). In the classification of Frost et al. (2001) most samples are alkali-calcic and ferroan.

Analytical methods

A total of 64 fresh samples were taken from the Krasnopol PIG-6 drill core from a depth range 621 – 1500 m. Chevkinite have also been identified in a few granitoid rock samples taken from the Filipów IG-1 and Pawłówka PIG-1A boreholes. The selection of CGM for microprobe study was performed using reflected-light optical microscopy (NIKON LV100) and electron microscopy with control of the qualitative chemical composition of minerals by means of an energy dispersive spectroscopy (Zeiss Sigma VP equipped with EDS Bruker XFlash 6|10 spectrometer). Identification of minerals under the reflected-light microscope was possible due to their large grain sizes (up to 0.5 mm), and by clear visible optical properties (reflectance slightly less than 20% and the presence of visible brown internal reflections).

The chemical compositions of the CGM and alteration products were determined using a CAMECA SX100 EPMA, equipped with four wavelength-dispersion spectrometers.. Operating conditions were as follows: 15 kV, beam current 40 nA or 20 nA (for altered grains only), beam-diameter range from 1- 5 μm depending on the size of analysed grains, 20 s and 10 s counting times for peak and background positions, respectively. Reference materials, selected analytical lines, diffracting crystals, and mean detection limits (quoted in wt%) were: Nb (metallic Nb, L_a, PET, 0.13); Ta (metallic Ta, M_a, TAP, 0.10); Si (diopside, K_a, TAP, 0.03); Ti (rutile, K_a, PET, 0.06); Zr (zircon, L_a, PET, 0.08); Th (ThO_2, M_a, PET, 0.10); U (UO_2, M_b, PET, 0.10); Al (orthoclase, K_a, TAP, 0.03); V(V_2O_5, K_a, LIF, 0.15); Sc (metallic Sc, K_a, LPET, 0.02); Y (YPO_4, L_a, TAP, 0.12); La (La-glass, L_a, LPET, 0.07); Ce ($CeP5O14$, L_a, LPET, 0.08); Pr (Pr-glass, L_b, LIF, 0.35); Nd ($NdGaO_3$, L_b, LIF, 0.46); Sm ($SmPO_4$, L_b, LIF, 0.46); Eu ($EuPO_4$, L_b, LIF, 0.25); Gd (GdP_5O_{14}, L_b, LIF, 0.49); Mg (diopside, K_a, TAP, 0.03); Ca (diopside, K_a, LPET, 0.02); Mn (rhodonite, K_a, LIF, 0.14), Fe (hematite, K_a, LIF, 0.12), Sr (celestine, L_a, LPET, 0.16); Ba (barite, L_a, PET, 0.14); Pb (crocoite, M_a, PET, 0.22); Na (albite, K_a, TAP, 0.07); K (orthoclase, K_a, PET, 0.04), and F (phlogopite, K_a, TAP, 0.81). The spectral interferences of the REE analytical lines were automatically corrected in the quantitative result files by the SX100 software. During the quantification procedure, the interference intensity of the overlapping lines calculated from the measurement on the calibrant material was taken into account. The raw data were reduced using the PAP-Φ(ρZ) procedure of Pouchou and Pichoir (1991).

Prior to EBSD examination, the sample was additionally polished (using a vibrating polisher) for 8 h in a diamond suspension with a grain diameter of 1/4 μm. The sample was covered with a 4.0 nm carbon layer for better surface discharge. EBSD patterns were collected with a Zeiss Auriga electron microscope equipped with a Brukere − FlashHR + detector with integrated ARGUS imaging device. The sample was tilted to 70° using the dedicated stage (tilt about sample X axis) for an optimal EBSD signal with working distance set to 19.15 mm, while the detector tilt angle was 2.42° and sample to detector distance of 15.02 mm. The experiments were carried out using an electron beam with an energy of 10 kV. Image tilt correction was used on the Zeiss SmartSEM software and no image rotation was applied. A single EBSD pattern of 320×240 resolution was recorded from the 0.86×0.86 μm area during 130 ms. The system was calibrated in Bruker ESPRIT 2. The pattern centre (PC), in Bruker fractional coordinates, was measured as: PC x = 0.506, PC y = 0.252 with a pattern aspect ratio of 1.33 (width/height). The hit rate of indexed pixels was 32.4%; the remaining part of the analysed sample was amorphous.

Results

Petrography

The host rocks

Petrographic descriptions of CMG-bearing samples from the Filipów IG-1 and Pawłówka PIG-1A cores can be found in Bagiński et al. (2001). The Krasnopol PIG-6 core monzodiorites and granodiorites hosting the CGM are coarse- and medium-grained with a well-developed porphyritic texture with plagioclase phenocrysts reaching up to 5 cm. The main minerals are plagioclase (An46 – An29), potassium feldspar, quartz, biotite [classified as phlogopite, with $Mg/(Mg + Fe_{tot})$ ratios of 0.52 – 0.57], amphibole [classified as hastingsite, with $Mg/(Mg + Fe_{tot})$ ratios of 0.57 – 0.61], clinopyroxene (classified as diopside, with Wo: 47–51, En: 33–37, Fs:14–19), Fe-Ti oxides and Fe-Cu sulphides (pyrrhotite, pyrite and chalcopyrite). The Krasnopol core is dominated by rocks with high contents of biotite and

amphibole. Clinopyroxene also occurs over the intervals 1002.8 – 1308.7 mand 1380.5 – 1500 m. The colour of the granitoids is variable; in the upper part of the section it is pink-grey, below the depth of 1112.8 mKrasnopol granitoids lack the pink colour, except at 1263.3 – 1308.7 m, where the granitoids are again reddish.

A notable feature of the rocks is the presence of fine-grained enclaves. These are usually dark in colour. The over-all size and form of the enclaves are difficult to define due to the fact that the rocks come from drill core; however, they commonly occur with monzodiorite/granodiorite at various depths. Compositionally they are monzonite, monzodiorite or monzogabbro. Usually they show non-oriented textures, are equigranular and occasionally contain large (up to 3 cm) K-feldspar or/and plagioclase (up to 0.5 cm) megacrysts. Sometimes they show a magmatic foliation, defined by mafic minerals. Enclaves are composed of the same miner-als as the surrounding rocks, differing only in their greater abundance of plagioclase and mafic minerals. The chemi-cal composition of enclave minerals is also similar to that of the host rock. The rocks matrix consist of 35–45 vol% plagioclase (An_{48-24}), 20–30 vol% phlogopite, with $Mg/(Mg + Fe_{tot})$ ratios of 0.53 – 0.64, 0–30 vol% clinopyroxene diopside, with Wo: 43–51; En: 33–37; Fs: 12–23 and 0–25 vol% hastingsite, with $Mg/(Mg + Fe_{tot})$ ratios of 0.56 – 0.63. Quartz and K-feldspar are interstitial and subordinate. Com-mon accessory minerals are magnetite and ilmenite, apatite, zircon and titanite.

The contacts of the enclaves with granodiorite are partly diffuse, lobate to crenulate. Large feldspar megacrysts are observed to cross the contacts between enclave and granod-iorite, in addition to occurring inside them. The plagioclase phenocrysts show poikilitic rims with mainly clinopyroxene and ilmenite inclusions. K-feldspar phenocrysts also have poikilitic rims with inclusions of plagioclase, clinopyroxene, biotite, apatite and ilmenite. The textural relationships are consistent with the mixing/mingling of two melts of different composition. Sample details are given in Table 1.

Chevkinite-group minerals

The CGM are common in samples of monzodiorites and granodiorites from Krasnopol PIG-6 drillcore (Nejbert et al. 2020). From 3 to 7 grains with a diameter of more than 100 µm were identified in a standard 6 cm^2 thin section. In addition, numerous small CGM inclusions, with sizes well below 10 µm, were observed within feldspars and biotite. The number of such inclusions is difficult to estimate; gener-ally during the study of standard thin sections, from 20 to 30 such grains were identified using scanning electron micros-copy–energy dispersive X-ray spectroscopy (SEM–EDS) methods. In samples identified as the richest in CMG, and/

or titanite-like phases formed after this mineral, they may constitute a maximum up to 0.03 vol%. The CGM are pre-sent in a wide variety of forms but the two most common are prismatic and platy. The prismatic types are usually between 50 and 100 µm long, which in our experience is unusually large for CGM (other than in pegmatites). They are bright [high average atomic number ($\overline{Z}$) contrast] on backscattered electrons (BSE) images and fairly homogeneous (Fig. 2a, b). The crystal in Fig. 2a is enclosed in magnetite showing ilmenite exsolution lamellae, those in Fig. 2b in alkali feld-spar, evidence that they were of magmatic crystallization. The spear-shaped crystal shown in Fig. 2c is patchily zoned, with high-$\overline{Z}$ material forming a residual part of the core and an extreme tip. The platy types are larger, up to 500 µm across, and usually patchily zoned from bright to vary dark. The crystal shown in Fig. 2d is unusual in being bright, but with a small, low $\overline{Z}$, core area and a dark rim which is asso-ciated with a patchily zoned grain. The core of the subhedral crystal in Fig. 2e is very complex and patchy, with a higher $\overline{Z}$ mantle where oscillatory zoning is just visible. The patchy core is more metamict than the rim due to a higher content of Th. The patchily zoned CGM at the left-hand edge of the crystal in Fig. 2f has been replaced towards the rims by an aggregate of a REE carbonate.

Textural features typical of magmatic crystallization are preserved in some crystals, such as the subhedral-euhedral form of certain prismatic crystals (Fig. 2a, b), crystals inter-grown with magmatic minerals (Fig. 2a, b), and those which display oscillatory zoning (Fig. 2e). Mainly, however, mag-matic zoning has been overprinted by hydrothermal altera-tion, recognizable by the development of patchy zones of lower $\overline{Z}$, as opposed to unaltered crystals which are invari-ably bright (high $\overline{Z}$) on BSE images.

The question arises as to why the degree of alteration was so variable, even within single thin sections. It seems that the unaltered crystals were protected by being enclosed within plagioclase crystals, e.g. in Fig. 2b. In contrast, the altered grains tended to occur along intergranular bounda-ries and were presumably involved in extensive intergranular fluid flow.

The CGM were also identified in granitoid samples from the Filipów IG-1 and Pawłówka PIG-1A boreholes. These occurred as large grains (up to about 100 µm), associated with Fe-Ti oxide aggregates and pyrrhotite, and fine, up to 10 µm, lamellar perrierite-(Ce) crystals appearing as fine, regularly distributed inclusions in plagioclase. In several large plagioclase crystals, a parallel arrangement of fine per-rierite grains was observed, which were also arranged paral-lel to the fine Fe-Ti oxides. In the samples from the Filipów IG-1 and Pawłówka PIG-1A boreholes, all the larger CGM grains were highly altered and broken down into titanite-like phases, allanite, REE-fluorocarbonates, and Ca-Fe carbon-ates. Only the small-sized lamellar perrierite-(Ce) inclusions

Fig. 2 Selection of representative BSE images of CGM-containing specimens. **a** Prismatic perrierite-(Ce) (Prr-Ce) intergrown with magnetite (Mag) showing ilmenite exsolution lamellae (Ilm). Sample Kr-6–33; analyses 1–10 in Table S1, Kr-6–33. **b** Prismatic perrierite-(Ce) embedded in alkali feldspar (Afs). Sample Fil-1, analyses in Table S2, Filipów 1. **c** Spear-shaped perrierite-(Ce) with patchy alteration (aPrr), sample Kr-6–41, analyses in Table S2, Kr-6–41. Ap – apatite. **d** Anhedral perrierite-(Ce) with dark altered core and rim, associated in the bottom part with a patchily zoned grain. Sample Kr-6–41, analyses 1–12 in Table S2, Kr-6–41. **e** Subhedral perrierite-(Ce) with oscillatory zoning and patchy core. Sample Kr-6–41, analyses 14–26 in Table S2. **f** The patchily zoned perrierite-(Ce) replaced towards the rims by an aggregate of a REE-carbonate (REE-Cb). Sample Pawłówka PIG-1A
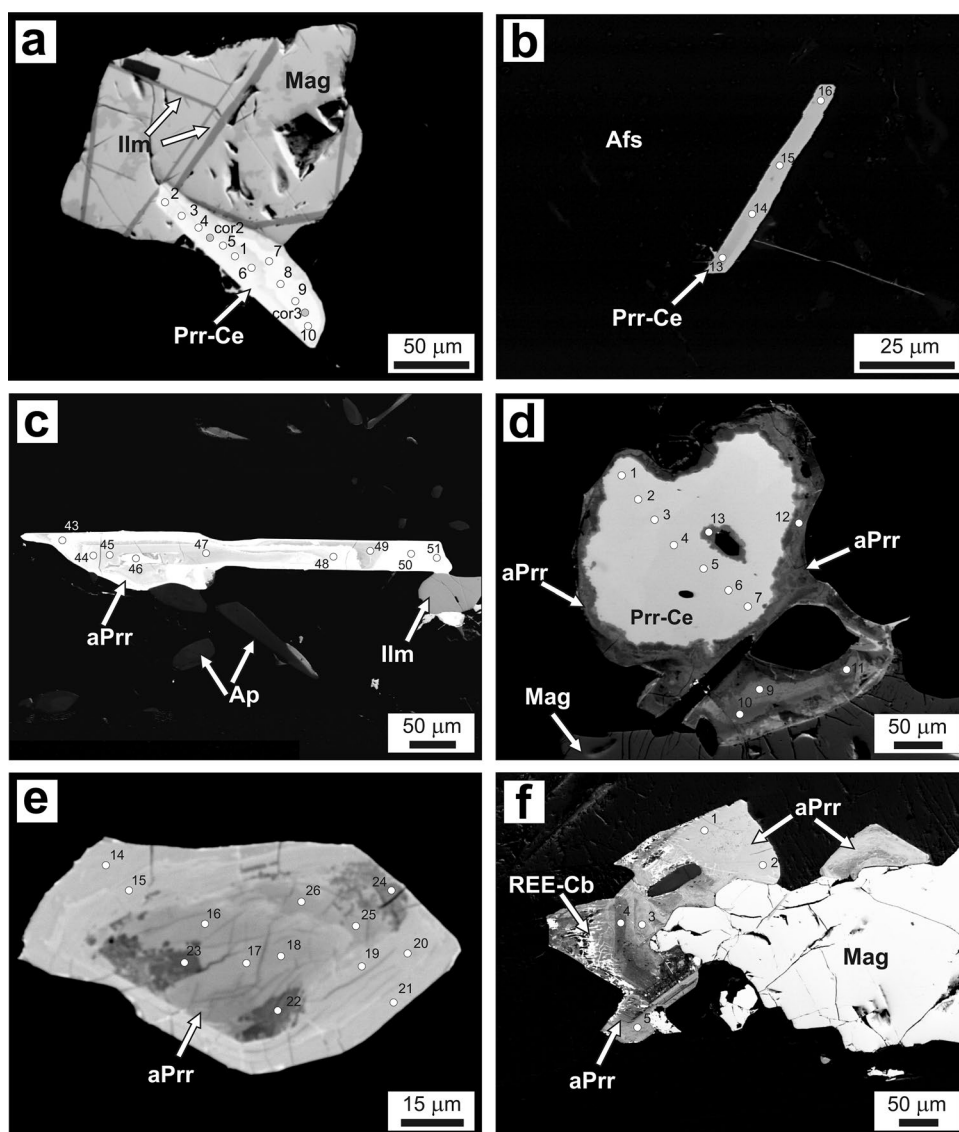
within plagioclase were relatively poorly altered as shown by their high brightness on the BSE images.

Composition of CGM

Perrierite-(Ce) compositions

Representative compositions of unaltered perrierite-(Ce) are given in Table 2; the full data set is given in Tables S1-S3 in the electronic supplementary material (ESM). Fluorine has been reported in the CGM, at levels up to 5.31 wt%. Belkin et al. (2009) argued that the F values determined by EPMA represent interference between the F-$K\alpha$ ($\lambda = 18.3199$ Å) and Ce-$M\xi$ ($\lambda = 18.3499$ Å) peaks. This, plus the uncertainty as to where F may be incorporated in the CGM structure, has resulted in the F values being reported in Tables S1-S3 but

not included in formula calculations. On the FeO* versus (CaO + SrO) (with FeO* = total Fe expressed as FeO) discrimination plot (Macdonald et al. 2009), they fall in the perrierite field (Fig. 3), with crystals from Filipów-1 showing slightly higher (CaO + SrO) values than those from Krasnopol PIG-6. Compositionally, they usually have analytical totals > 95 wt% and are close to the stoichiometric formula $A_4BC_2Ti_2(Si_2O_7)_2O_8$. Cations have been allocated to structural sites as follows: A—REE, Ca, Y, Sr, Th, B—Fe^{2+}, C—Fe^{2+}, Mn, Mg, Al, V, Sc, Zr, Nb, Ta, Ti; D—Ti; T—Si. Recent work has shown that in some CGM cations may not enter the standard structural sites. For example, Stachowicz et al. (2019) allocated some Nb and Mg to the D site in their study of Nb-rich chevkinite-(Ce) from the Biraya rare-metal deposit, Russia, and Nagashima et al. (2020) allocated some Th to the B (M1) site in chevkinite-(Ce) from Ashizuri, Japan. However, in the current case the allocations result in

Table 2 Representative chemical compositions and calculated mineral formulae of unaltered perrierite-(Ce)

Sample	Kr-6–59	Kr-6–59	Kr-6–59	Kr-6–41	Kr-6–41	Kr-6–41	Kr-6–33	Kr-6–2
Analysis	1	2	3	4	5	6	7	8
Major constituents (wt%)								
Nb_2O_5	0.08	bdl	0.09	bdl	bdl	bdl	bdl	bdl
Ta_2O_5	0.09	0.19	0.08	0.15	0.15	bdl	0.12	0.08
SiO_2	20.69	20.64	20.34	20.52	20.19	20.85	20.55	20.70
TiO_2	17.66	17.77	18.28	18.12	18.50	18.99	17.89	18.58
ZrO_2	0.59	0.61	0.51	0.70	0.49	0.98	0.41	1.54
ThO_2	2.17	2.86	0.34	2.52	0.10	0.08	1.37	1.54
Al_2O_3	3.80	3.86	3.83	3.81	3.90	3.79	4.02	4.12
V_2O_3	0.15	0.12	0.19	0.32	0.15	0.18	0.11	0.15
Sc_2O_3	0.29	0.27	0.45	0.23	0.40	0.38	0.37	0.39
Y_2O_3	0.31	0.30	0.26	0.26	0.30	0.34	0.35	0.29
La_2O_3	10.05	10.03	9.84	9.93	9.83	9.70	10.97	9.34
Ce_2O_3	19.18	18.99	19.28	19.12	19.32	19.08	20.08	17.16
Pr_2O_3	1.44	1.41	1.69	1.37	1.68	1.49	1.57	1.46
Nd_2O_3	5.68	5.97	5.75	5.29	5.82	5.61	6.29	5.51
Sm_2O_3	0.45	0.39	0.26	0.27	0.51	0.60	0.48	0.44
Eu_2O_3	0.56	0.44	0.52	0.48	0.62	0.54	-	0.40
Gd_2O_3	0.24	0.24	bdl	bdl	0.36	0.28	bdl	0.24
MgO	0.68	0.75	0.61	0.66	0.61	0.49	0.80	0.51
CaO	5.21	5.18	5.18	5.22	5.34	5.44	4.91	5.99
MnO	bdl	0.08	bdl	bdl	bdl	bdl	0.10	bdl
FeO*	6.90	7.18	6.95	7.12	7.18	6.51	6.91	6.43
SrO	0.10	-	0.03	-	-	-	-	-
BaO	bdl	bdl	0.17	bdl	bdl	bdl	-	0.21
F	bdl	bdl	bdl	bdl	bdl	bdl	bdl	bdl
Sum	96.32	97.28	94.65	96.09	95.45	95.33	97.30	95.08
$\Sigma\ REE_2O_3$	37.60	37.47	37.32	36.46	38.14	37.30	39.38	34.55
Calculated formulae (apfu)*								
Ca	1.115	1.103	1.115	1.115	1.141	1.147	1.043	1.268
Sr	0.012	-	0.004	-	-	-	-	-
Ba	0.000	0.000	0.014	0.000	0.000	0.000	0.000	0.016
Y	0.033	0.032	0.028	0.027	0.032	0.036	0.037	0.031
La	0.741	0.735	0.729	0.730	0.723	0.704	0.801	0.681
Ce	1.403	1.381	1.418	1.396	1.411	1.375	1.457	1.242
Pr	0.105	0.102	0.123	0.100	0.122	0.107	0.113	0.105
Nd	0.405	0.424	0.412	0.376	0.414	0.394	0.445	0.389
Sm	0.031	0.027	0.018	0.018	0.035	0.041	0.033	0.030
Eu	0.038	0.030	0.036	0.033	0.042	0.036	0.000	0.027
Gd	0.016	0.016	0.000	0.000	0.024	0.018	0.000	0.016
Th	0.099	0.129	0.015	0.114	0.005	0.004	0.062	0.069
Sum A	3.996	3.978	3.911	3.910	3.948	3.861	3.991	3.874
$Fe^{2+}\ (=B)$	1.000	1.000	1.000	1.000	1.000	1.000	1.000	1.000
Fe^{2+}	0.153	0.193	0.167	0.187	0.197	0.071	0.145	0.063
Mn	0.000	0.013	0.000	0.000	0.000	0.000	0.016	0.000
Mg	0.203	0.221	0.183	0.196	0.181	0.144	0.237	0.151
Al	0.895	0.903	0.906	0.894	0.917	0.879	0.939	0.960
V	0.023	0.019	0.031	0.052	0.024	0.028	0.018	0.024
Sc	0.050	0.047	0.079	0.040	0.069	0.065	0.064	0.067
Zr	0.057	0.059	0.050	0.000	0.048	0.094	0.040	0.148
Nb	0.008	0.000	0.008	0.068	0.000	0.000	0.003	0.000

Table 2 (continued)

Sample	Kr-6–59	Kr-6–59	Kr-6–59	Kr-6–41	Kr-6–41	Kr-6–41	Kr-6–33	Kr-6–2
Analysis	1	2	3	4	5	6	7	8
Ta	0.057	0.059	0.050	0.008	0.008	0.000	0.007	0.002
Ti	0.654	0.654	0.761	0.718	0.774	0.810	0.665	0.761
Sum C	2.100	2.169	2.235	2.162	2.218	2.091	2.133	2.176
Ti (=D)	2.000	2.000	2.000	2.000	2.000	2.000	2.000	2.000
Si (=D)	4.132	4.099	4.085	4.091	4.026	4.102	4.071	4.092
Σ cations	13.23	13.25	13.23	13.16	13.18	13.05	13.23	13.14

Calculated based on 22 O atoms per formula unit. Na_2O, K_2O and PbO below detection in all samples. FeO, all Fe as Fe^{2+}. Dash—not determined. bdl, below detection limit

near-stoichiometric formulae: A—3.85 – 4.0 (average 3.9) apfu; B—1.0 apfu; C – 2.0 – 2.25 (2.15) apfu; D—2.0 apfu, Si—4.1 – 4.15 (4.1) apfu and cation sums are in the range 13.1 – 13.25 (13.2) apfu. It may be inferred that the cation allocations are a fair representation of their distribution in the natural minerals.

Variations in the abundances of the major components are modest, e.g. SiO_2 20.2 – 20.9 wt%, TiO_2 17.7 – 19.0 wt% and Ce_2O_3 17.2 – 20.1 wt%. Those in the minor components are larger, e.g. ThO_2 0.1 – 2.9 wt% and ZrO_2 0.4 – 1.5 wt%. The exceptionally high values of ThO_2 in a crystal in sample Kr-6–33, ≤ 9.10 wt% (Table S1; Fig. 2a), match those in perrierite-(Ce) from the rhyolitic Joe Lott

Fig. 3 Composition of unaltered CGM plotted in the discrimination plot of Macdonald et al. (2009). Data from Tables S1–S3

Tuff, Utah (Galanciak et al. 2020) in being among the highest yet recorded in the CGM. An important feature is that Al is the dominant cation in the C site. This feature has previously been recorded in perrierite in high-grade metamorphic rocks from Antarctica and India (Harley 1994; Hokada 2007; Belkin et al. 2009), and in chevkinite in albitites from Siberia (Proschenko 1967) and the Pyrenees (Monchoux et al. 2006) (Fig. 4).

Chondrite-normalized REE plots (Fig. 5) show decreases from La to Sm, with a significant variation in La_N/Sm_N values (6 – 24), and strong positive Eu anomalies (Eu/Eu* 1.7 – 5.1, with two outliers at 9.5 and 10.8). However, the ranges may partly reflect Sm, Eu and Gd values close to the EPM detection limits. Positive Eu anomalies might be a result of plagioclase breakdown during the observed sericitisation process (Zozulya et al. 2020).

Hydrothermal alteration trends

Compositions of altered CGM are given in Table 3 and Tables S1-S3. Previous studies of the hydrothermal alteration of CGM, summarized in Bagiński et al. (2015) and Macdonald et al. (2019) have shown that invariable compositional features of the process are low analytical totals and non-stoichiometric formulae. These features also mark the Mazury Complex CGM. Analytical totals are always less than 95 wt% and as low as 85 wt%, the low values presumably reflecting water absorbed into the structure and/or the presence of vacancies. Sums of cations are as low as 12.2 apfu. Data for altered crystals initially follow a trend of decreasing Fe contents at about constant Ca content until at 3 wt% CaO they diverge into two trends. One, an initial Fe-depletion trend, varies between specimens; in Kr-6–41, for example, a slight increase in CaO reverses at FeO* 4.5 wt%, followed by rapid Fe and Ca depletion to < 2 wt% CaO, while in Filipów-1, the earliest alteration phase resulted in Ca depletion before the trend involved strong depletion in Ca and Fe to ~ 2 wt% CaO (Fig. 6a). Other features of this part of the trend include decreases in Si, Al and Mg contents and increasing Ti. In Kr-6–41 REE
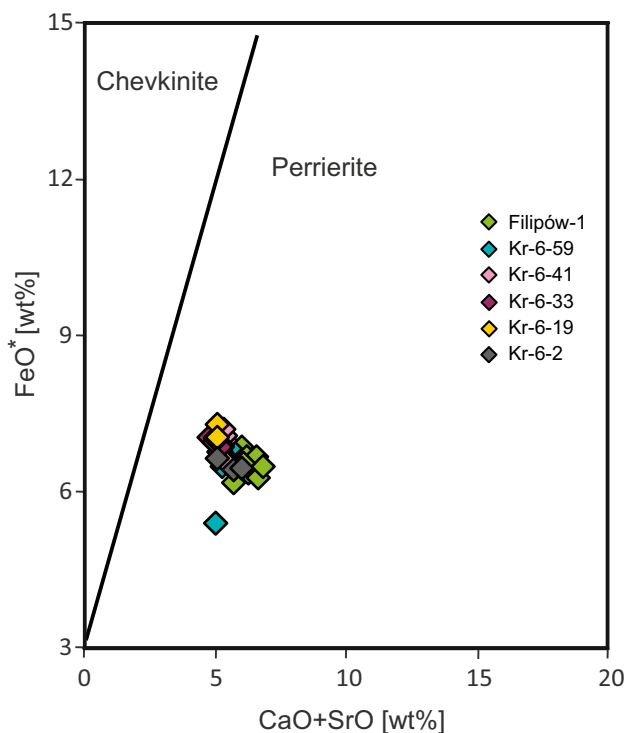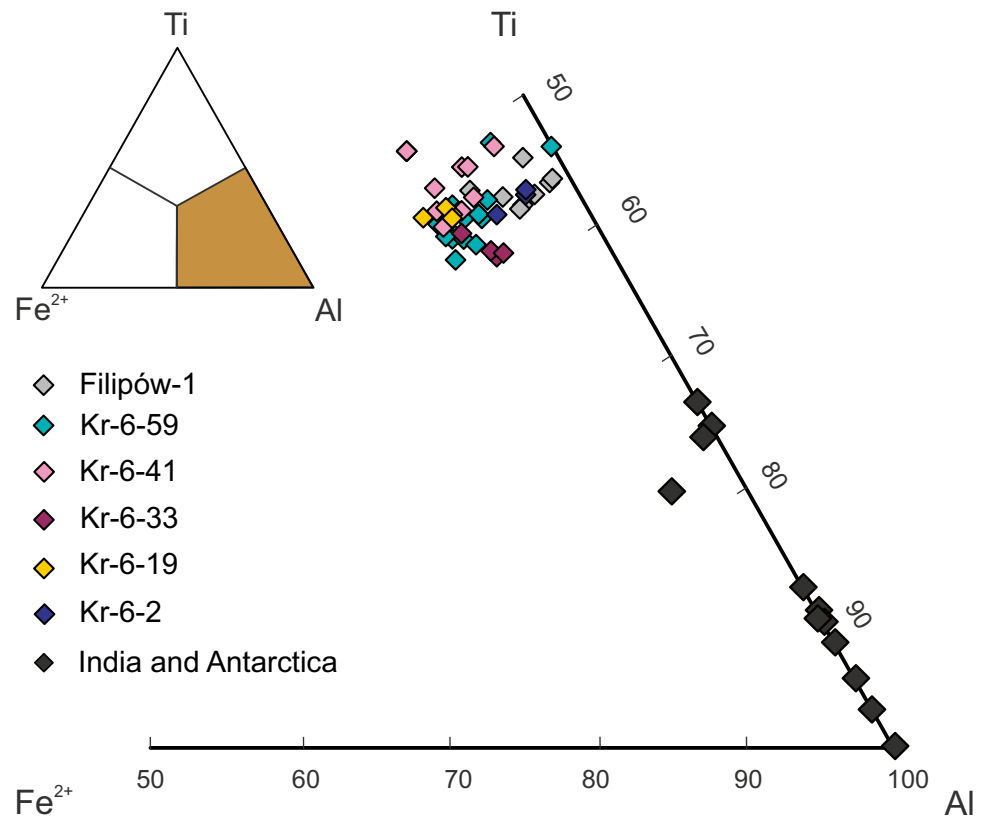
Fig. 4 Plot of Ti-Fe^{2+}-Al in C site of unaltered crystals, showing the dominance of Al. Data from Tables S1–S3. Perrierites from granulites from India and Antarctica plotted for comparison (Belkin et al. 2009, Table 1). Values are plotted in apfu

abundances decrease along the trend, whereas in Filipów-2, REE increase along it.

The main feature of compositions along the second trend is the increasing contents of Ti, Ca (Fig. 6b) and Si at about constant Fe. Other features are the increasing Al and decreasing contents of REE, Y, Mg, Sc and Zr. The REE$_2$O$_3$ contents, for example, which total ~ 36 – 38 wt% in the unaltered CGM, are < 5 wt% in the most altered samples: this is discussed in more detail below.

There are minor variants on the alteration schemes described above. For example, in Kr-6–19 two low Ti-Ca
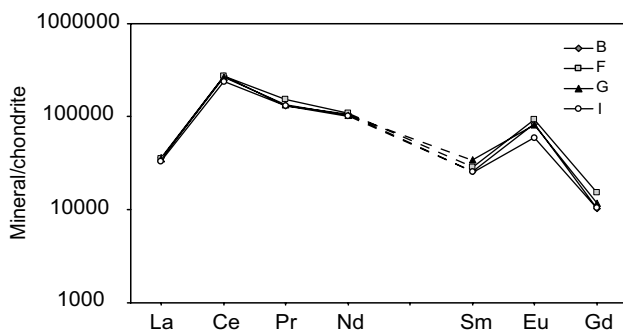

Fig. 5 Chondrite-normalized REE plots for representative unaltered perrierite-(Ce). Data from Table 2. Normalizing factors after Sun and McDonough (1989)

analyses (Table 3 and S1; analyses 53, 54) have high Fe (12.61, 11.21 wt% FeO*) and low REE (20.08 wt% REE$_2$O$_3$). In Fig. 6a, b for unusually Fe-rich altered analyses plot with the unaltered types (arrowed). Two other low Ti-Ca analyses (30, 34) have low Fe (0.90, 0.93 wt% FeO*) and high REE (44.62, 48.96 wt% REE$_2$O$_3$). All these analyses have high F contents (2 – 5 wt%) and it is possible that this has resulted in some unusual element redistribution. Alternatively, the compositional features may be related to the nature of other accessory minerals forming during the alteration.

Extrapolation of Ti, Si and Ca values in the second trend coincide with the composition of titanite (Fig. 6b). The two analyses closest to titanite are from Kr-6–19 (Table S1; analyses 63, 64). The average formula, calculated on the basis of 5 oxygens, is $[Ca_{0.88}\Sigma(La–Nd)_{0.04}Sr_{0.02})_{0.94}$ $(Ti_{0.75}Al_{0.20}Fe^{2+}_{0.03})_{0.98}Si_{1.09}]$, with the sum of cations = 3.04, i.e. the phase is compositionally close to titanite, $CaTiOSiO_4$, with some replacement of Ti by Al. The Al levels are significant ($\leq$ 5 wt% Al$_2$O$_3$) but not exceptional: Seifert and Kramer (2003), for example, recorded values of Al$_2$O$_3$ up to ~ 15 wt% in titanite from lamprophyres of the Variscan orogeny in Germany. In comparison, Jiang et al. (2006) reported 3.99 wt% Al$_2$O$_3$ in titanite in an allanite-ilmenite-titanite mantle on altered chevkinite-(Ce) in the Shuiquangou syenite, China. Additionally Vlach et al.

Table 3 Representative compositions of altered CMG

Table 3 (continued)

Sample	Kr-6–19	Kr-6–19	Kr-6–19	Kr-6–19
Analysis	53	54	63	64
Major constituents (wt%)				
Nb_2O_5	bdl	bdl	bdl	bdl
Ta_2O_5	0.15	0.12	bdl	bdl
SiO_2	26.73	25.78	31.66	31.70
TiO_2	15.28	14.53	29.19	28.69
ZrO_2	1.18	1.15	0.31	0.40
ThO_2	0.56	0.61	0.31	0.33
Al_2O_3	4.16	3.41	4.90	5.02
V_2O_3	0.33	0.23	0.16	0.24
Sc_2O_3	1.48	1.55	0.16	0.19
Y_2O_3	bdl	bdl	bdl	bdl
La_2O_3	4.76	5.07	0.20	0.35
Ce_2O_3	10.79	11.93	1.70	1.86
Pr_2O_3	0.98	0.85	0.16	0.22
Nd_2O_3	2.96	3.82	0.53	0.84
Sm_2O_3	0.28	0.32	bdl	bdl
Eu_2O_3	bdl	bdl	bdl	bdl
Gd_2O_3	0.30	bdl	bdl	bdl
MgO	1.67	1.39	0.02	0.02
CaO	5.67	7.57	23.85	23.95
MnO	0.44	0.48	bdl	bdl
FeO*	12.61	11.21	1.22	1.15
SrO	0.27	0.32	bdl	bdl
BaO	0.39	0.35	0.15	0.15
Na_2O	0.31	0.18	0.13	0.17
K_2O	0.16	0.15	0.03	bdl
F	2.87	5.31	1.16	1.00
Total	91.46	91.00	94.68	95.28
F	2.87	5.31	1.16	1.00
ΣREE_2O_3	20.08	22.00	2.59	3.27
Calculated formulae (apfu)*				
Ca	1.125	1.541	3.867	3.878
Sr	0.029	0.035	0.064	0.064
Na	0.110	0.067	0.038	0.050
K	0.037	0.035	0.006	0.000
Ba	0.028	0.026	0.009	0.009
Y	0.000	0.000	0.000	0.000
La	0.325	0.355	0.011	0.020
Ce	0.732	0.830	0.094	0.103
Pr	0.066	0.059	0.009	0.012
Nd	0.196	0.259	0.029	0.045
Sm	0.018	0.021	0.000	0.000
Eu	0.000	0.000	0.000	0.000
Gd	0.019	0.000	0.000	0.000
Th	0.023	0.026	0.011	0.011
Sum A	2.709	3.255	4.138	4.192
Fe^{2+}	1.000	1.000	0.154	0.145
Mn	0.000	0.000	0.000	0.000
Mg	0.000	0.000	0.005	0.005
Sum B	1.000	1.000	0.159	0.150
Fe^{2+}	0.953	0.781	0.000	0.000
Mn	0.069	0.078	0.000	0.000
Mg	0.461	0.393	0.000	0.000
Al	0.908	0.764	0.874	0.894
V	0.049	0.035	0.019	0.029
Sc	0.239	0.257	0.021	0.025
Zr	0.107	0.106	0.023	0.029
Nb	0.000	0.000	0.000	0.000
Ta	0.007	0.006	0.000	0.000
Ti	0.128	0.075	1.322	1.260
Sum C	2.922	2.494	2.259	2.238
Ti (= D)	2.000	2.000	2.000	2.000
Si (= T)	4.949	4.898	4.791	4.790
Σ cations	13.58	13.65	13.35	13.37

Calculated based on 4 O atoms per formula unit. FeO, all Fe as Fe^{2+}. bdl, below detection limit

(2014) suggested that allanite growth is favored by relatively high oxidizing conditions.

Structural breakdown of perrierite

It appears that the Mazury Complex CGM have recorded intermediate stages in the alteration of a CGM to a titanite-like phase. We have carried out detailed EPMA and EBSD analyses in an attempt to determine the compositional and structural nature of the titanite-like phase. Five compositional profiles were made across the crystal in sample Kr-6–41 shown in Fig. 7a; the data are given in Table S2. Compositional variations along one profile, as an example (profile E–F), are shown in Fig. 8. The crystal has been divided into three zones, the bright, transitional and dark zones. The bright zone is slightly altered perrierite-(Ce), brighter spots pointing to local concentrations of Ti (Fig. 9). Within the transitional zone, there are increases in the contents of SiO_2, TiO_2, and ThO_2, and decreases in FeO*, SrO, BaO, which are continued into the dark zone. Most marked is the sharp drop into the dark zone of LREE (La – Eu), from $\Sigma REE_2O_3 \geq 35$ wt% to < 5 wt%. While the most Ti–rich analyses have a titanite-like composition, there is a notable gap between 5 and 14 wt% CaO, the gap coinciding precisely with the transition zone. Thus the transition from perrierite-(Ce) to titanite-like compositions was sharp. The gap does not exist in all crystals in the data set; for example, there is a continuous series of compositions in sample Kr-6–19 (Table S1). Judging from the patchiness of the partially altered perrierite-(Ce), the alteration reached different parts
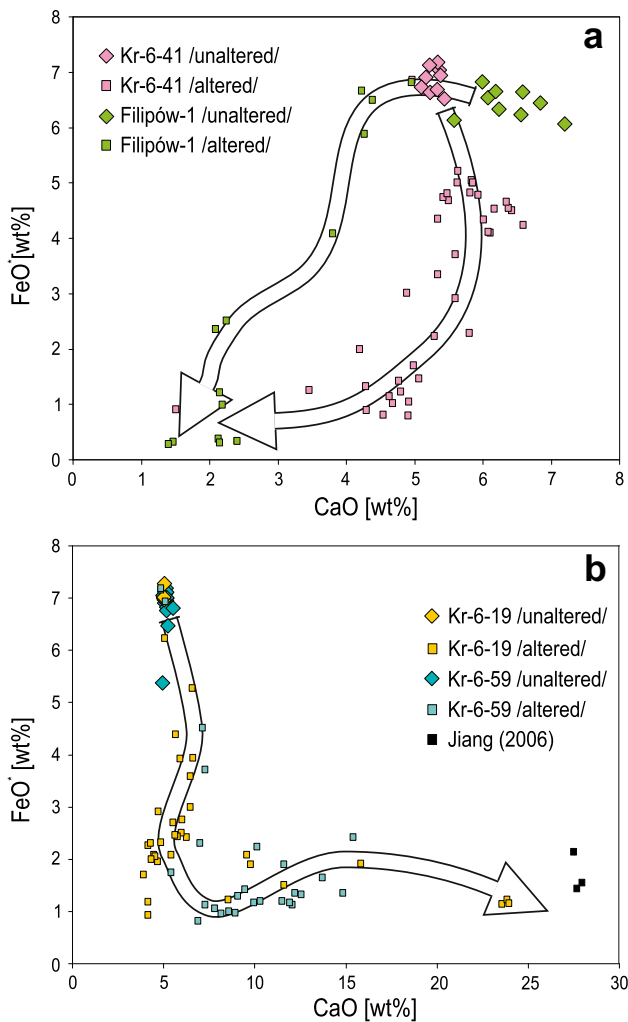
Fig. 6 a Two Ca-Fe depletion trends exemplified by samples Kr-6–41 and Filipów-1. **b** The Ca-Ti enrichment trend as shown by Kr-6–19 and Kr-6–59. Data from Tables S1 and S2. Also plotted is the composition of titanite formed by breakdown of chevkinite-(Ce) in the Shuiquangou syenitic intrusion, China (Jiang 2006)
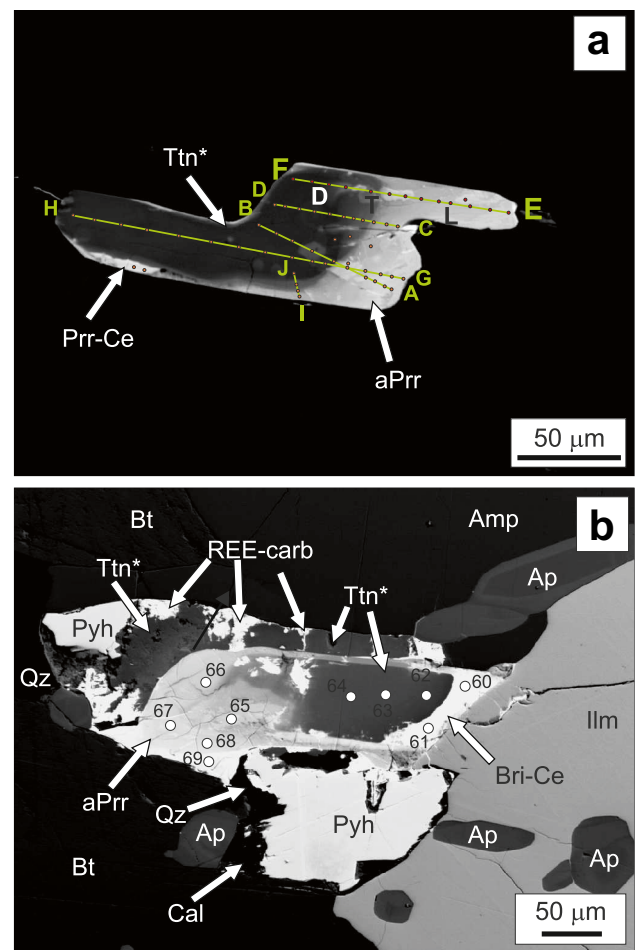

Fig. 7 a BSE image of perrierite-(Ce) showing locations of compositional profiles (sample Kr-6–41; analyses in Table S2). **b** BSE image of sample Kr-6–19, showing partially replaced perrierite-(Ce), the titanite-like phase (Ttn*), pyrrhotite (Pyh), REE carbonates (REE-carb) and britholite-(Ce) (Bri-Ce). Amp, amphibole: Bt, biotite: Cal, calcite: Qz, quartz. D – dark, T – transitional, L – light

of the crystals at different times. The breakdown of perrierite-(Ce) was clearly a very variable process. Furthermore, the different alteration trends shown on Fig. 6 may indicate that fluids of different composition affected the rocks at different times.

The crystal shown in Fig. 7b is of particular interest because it provides evidence of the nature of the hydrothermal fluids promoting the alteration to the titanite-like phase, the presence of REE-carbonates and pyrrhotite points to the presence of CO_2 and S in the fluids.

A representative electron backscatter pattern of perrierite-(Ce), crystallizing in $P2_1/c$ (a standard setting of commonly used, $P2_1/a$, the difference is only in the order of the crystallographic axes, both choices are symmetrically equivalent) is presented together with indexed, simulated pattern in Fig. 12.

Compositional data in Fig. 8, between analyses 22 – 28 correspond to the crystalline section of perrierite-(Ce) obtained from EBSD (red zone in Fig. 10a). Perrierite-(Ce) breaks down to an amorphous phase of titanite-like composition. Figure 10b shows the crystalline areas in brighter colour. The interior of the analyzed surface, i.e. the titanite-like phase, does not diffract electrons, meaning that it is amorphous.

Discussion

Crystallization conditions

The perrierite-bearing rocks from the Mazury Complex crystallized from broadly mafic to trachyandesitic melts. This is consistent with the findings of Macdonald and Belkin

Fig. 8 Compositional variations along profile E–F of crystal from sample Kr-6–41 shown in Fig. 7a (analyses in Table S2)
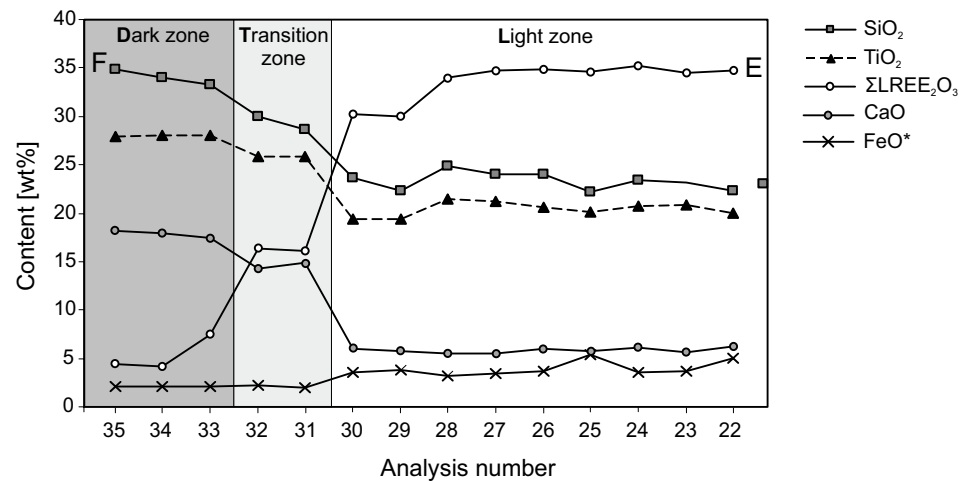
(2002), who showed that in igneous suites perrierite tends to form in rocks of intermediate and mafic composition (Fig. 11) while chevkinite forms in more evolved melts, such as granites, syenites and extrusive equivalents. Information on the P–T crystallization conditions comes from the associated charnockitic rocks. Based on pyroxene compositions, (Bagiński and Krzemińska 2005; Bagiński et al. 2006) estimated that the charnockites crystallized at a maximum range of ca. 850 – 950 °C and under variable polybaric pressure conditions. This temperature range is consistent with the likely crystallization temperatures of intermediate melts. Note, however, that the estimates assumed limited thermal influence from the coeval anorthosite bodies, intruded during the same AMCG magmatism stage.

Crystallization of the perrierite-(Ce) in the granulite facies is consistent with the occurrence of dominant Al in the C site. Al-dominant perrierite has been reported from several areas of granulitic facies rocks in Antarctica and India (Harley 1994; Hokada 2007; Belkin et al.

2009) (Fig. 4). There is also experimental evidence that high-pressure appears to favour the entry of Al into the CGM structure: Green and Pearson (1988) crystallized Al-dominant perrierites-(Ce) from REE-enriched andesitic and rhyolitic melts at P = 20 kbar, T = 1050 °C.

Effects of hydrothermal activity

Studies of the hydrothermal alteration of chevkinite-(Ce) from Russia and Scotland (Bagiński et al. 2015) and Brazil

Fig. 10 **a** BSE image of Kr-6–41 sample with imposed phase map of perrierite-(Ce) from EBSD analysis. **b** Pattern quality map indicating the size of the analyzed surface where brightness of the pixels reflects the relative quality of the collected diffraction patterns. The internal part of the compositionally titanite-like phase is non-crystalline, showing no diffraction

Fig. 9 Ti Kα x-ray intensity map for crystal shown in Fig. 7a. The colour range from blue to red indicates increasing concentrations of Ti
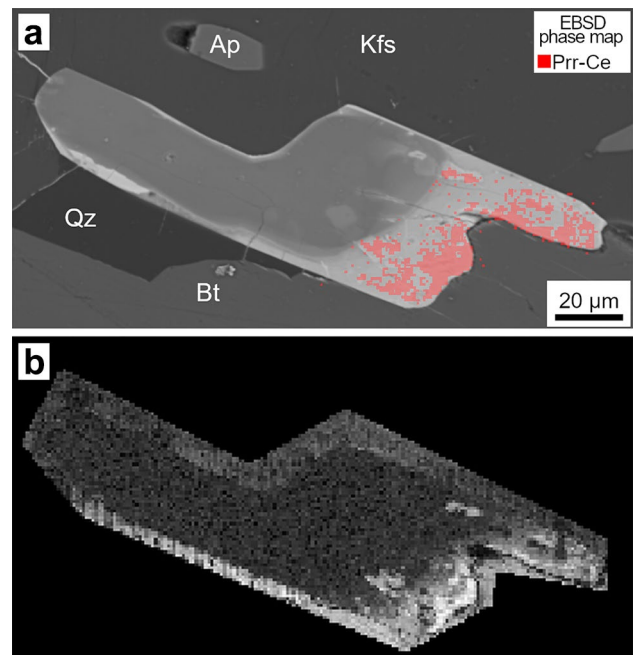
Fig. 11 Unaltered perrierite-(Ce) in the paragenesis plot of Macdonald and Belkin (2002), slightly modified. Values are plotted in apfu
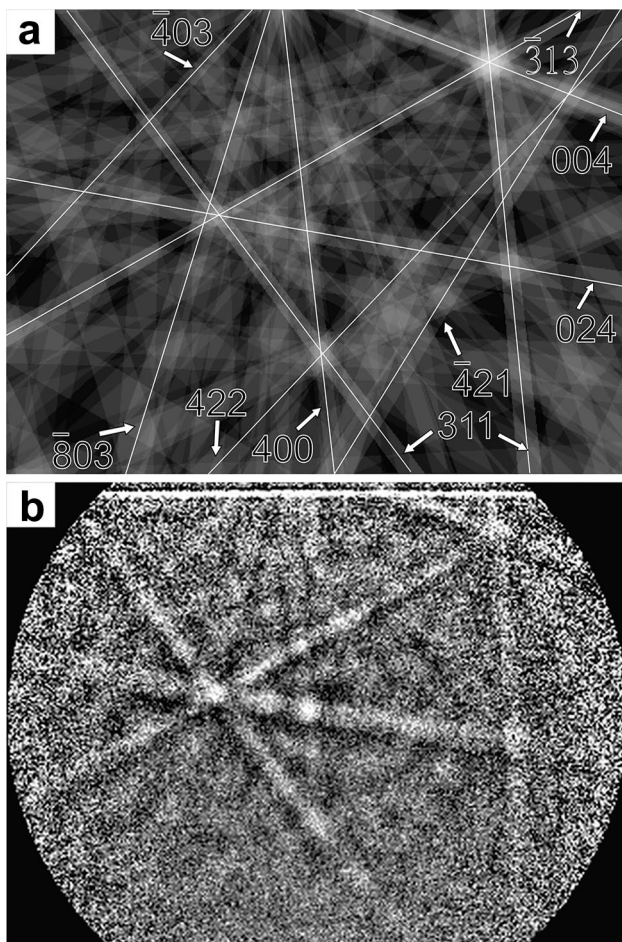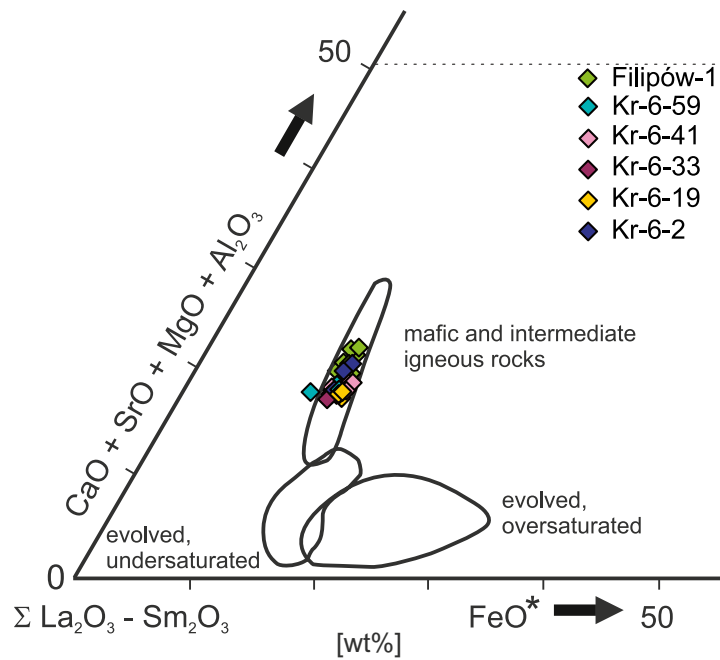

Fig. 12 **a** Simulated, indexed electron backscatter pattern of perrierite-(Ce). **b** Corresponding, representative experimental pattern

(Vlach and Gualda 2007) found that progressive alteration led initially to Ca enrichment at constant Ti and then to rapid Ca depletion with strong Ti enrichment. REE behaviour was more variable, being enriched in some crystals, depleted in others. The Ca, REE, Si and Fe were removed in the fluid phase. The types of alteration shown in Fig. 6a are, however, broadly similar to that recorded by Bagiński et al. (2015). The second trend involved enrichment in Ca, Ti and Si and strong depletion in REE and Y. The breakdown of CGM to a titanite-like phase in a wide range of natural rocks (e.g. gabbroids, syenites, pegmatites and metasomatites) has been recorded by, *inter alios*, Jiang (2006), Prol-Ledemsa et al. (2012), Macdonald et al. (2015a, b), Bagiński et al. (2016) and Spiridonov et al. (2019). In none of these studies was the identification of the titanite-like phase made on the basis of a structural analysis. The Krasnopol case raises the question as to whether the other examples are truly crystalline.

The alteration sequences and products were highly variable between crystals; it may be inferred that the variations were at least partly related to variable compositions of the hydrothermal fluids. Those described by Macdonald et al. (2015b) and Bagiński et al. (2016) were alkaline and contained significant CO_2 and F, whereas those in Macdonald et al. (2015a) were thought to have been acidic, with significant CO_2 but poor in F. The crystal shown in Fig. 7b is of particular interest because it provides evidence of the nature of the hydrothermal fluids promoting the alteration at Krasnopol. The presence of REE-carbonates and calcite (Figs. 2f, 7b) shows that the fluids were CO_2-bearing, while the pyrrhotite points to a component of S. The high F contents (up to 5 wt%) of some altered CGM and its presence

in the REE-carbonate further suggest that the fluids were F-bearing. We can speculate that the titanite-like phase would eventually have crystallized to titanite. Possibly the temperatures during hydrothermal alteration were simply too low to form it but we note that titanite can form at very low temperatures: in an extreme case, it has been recorded as a result of microbial alteration of volcanic glass (Izawa et al. 2019). Alternatively, it may have been a function of the duration of the alteration episode.

Conclusions

Perrierite-(Ce), a member of the chevkinite-group of minerals, is present in monzodiorites and granodiorites of the Mesoproterozoic Krasnopol intrusion, formed under granulite facies conditions. Consistent with a high-pressure origin, Al is dominant at the C site. The perrierite-(Ce) was extensively altered by hydrothermal fluids, which were CO_2 and F-bearing, with a component of S. At least two alteration schemes, involving different element mobilities, have been identified, perhaps indicating the presence of more than phase of alteration. One scheme resulted in an amorphous phase compositionally close to titanite.

References

Bagiński B, Duchesne JC, Vander Auwera J, Martin H, Wiszniewska J (2001) Petrology and geochemistry of rapakivi-type granites from the crystalline basement of NE Poland. Geol Quart 45:33–52

Bagiński B, Krzemińska E (2005) Various kinds of charnockitic rocks from NE Poland. Mineral Soc Pol-Spec Pap 26:13–17

Bagiński B, Kozłowski A, Krzemińska E (2006) Fluid inclusion studies – the only key to estimatethe crystallization conditionsof charnokitic rocks from selected boreholes from NE Poland ? Mineral Pol-Spec Pap 29:83–86

Bagiński B, Macdonald R, Dzierżanowski P, Zozulya D, Kartashov PM (2015) Hydrothermal alteration of chevkinite-group minerals: products and mechanisms. Part 1. Hydration of chevkinite-(Ce). Mineral Mag 79:1019–1037

Bagiński B, Zozulya D, Macdonald R, Kartashov PM, Dzierżanowski P (2016) Low-temperature hydrothermal alteration of a rare-metal rich quartz-epidote metasomatite from the El'ozero deposit, Kola Peninsula, Russia. Eur J Mineral 28:789–910

Belkin HE, Macdonald R, Grew ES (2009) Chevkinite-group minerals from granulite-facies metamorphic rocks and associated pegmatites of East Antarctica and South India. Mineral Mag 73:149–164

Claesson S, Sundblad K, Ryka W, Moczydłowska M, Reinfrank R (1995) Proterozoic ages from the Precambrian of Poland – results and implications. In: Glebovitsky VA, Kotov AB: MAEGS-9 (eds) Precambrian of Europe. Abstract 21

Dörr W, Belka Z, Marheine D, Schastok J, Valverde-Vaquero P, Wiszniewska J (2002) U-Pb and Ar-Ar geochronology of anorogenic granite magmatism of the Mazury complex NE Poland. Precamb Res 119:101–120

Duchesne JC, Martin H, Bagiński B, Wiszniewska J, Vander Auwera J (2010) The origin of ferroan-potassic A-type granitoids: the case of the hornblende-biotite granite suite of the Mesoproterozoic Mazury complex, northeastern Poland. Can Mineral 48:947–968

Frost BR, Barnes CG, Collins WJ, Arculus RJ, Ellis DJ, Frost CD (2001) A geochemical classification for granitic rocks. J Petrol 42(11):2033–2048

Galanciak J, Bagiński B, Macdonald R, Belkin HE, Kotowski K, Jokubauskas P (2020) Relationships between monazite, apatite and chevkinite-group minerals in the rhyolitic Joe Lott Tuff, Utah, USA. Lithos 354–355, 105349

Green TH, Pearson NJ (1988) Experimental crystallization of chevkinite/ perrierite from REE-enriched silicate liquids at high pressure and temperature. Mineral Mag 52:113–120

Haapala I, Rämö OT (1992) Tectonic setting and origin of the Proterozoic rapakivi granites of southeastern Fennoscandia. Trans Roy Soc Edinburgh: Earth Sci 83:165–171

Haapala I, Rämö OT (1999) Rapakivi granites and related rocks: an introduction. Precamb Res 95:1–7

Haapala I, Rämö OT, Frindt S (2005) Comparison of Proterozoic and Phanerozoic rift–related basaltic–granitic magmatism. Lithos 80:1–32

Harley SL (1994) Mg-Al yttrian zirconolite in a partially melted sapphirine granulite Vestfold Hills, East Antarctica. Mineral Mag 58:259–269

Hokada T (2007) Perrierite in sapphirine-quartz gneiss: geochemical and geochronological features and implications for accessory-phase paragenesis of UHT metamorphism. J Mineral Petrol Sci 102:44–49

Izawa MRW, Bannerjee NR, Shervais JW, Flemming RL, Hetherington CJ, Muehlenbachs K, Schultz C, Das D, Hanan BB (2019) Titanite mineralization of microbial bioalteration textures in Jurassic volcanic glass., Coast Range ophiolite, California. Front Earth Sci 2019. https://doi.org/10.3389/feart.2019.00315

Jiang N (2006) Hydrothermal alteration of chevkinite-(Ce) in the Shuiquangou syenitic intrusion, northern China. Chem Geol 227:100–112

Kubicki S, Ryka W (eds) (1982) Atlas geologiczny podłoża krystalicznego polskiej części platformy wschodnioeuropejskiej. Wydawnictwa Gelogiczne Warszawa

Macdonald R, Belkin HE (2002) Compositional variation in minerals of the chevkinite group. Mineral Mag 66:1075–1098

Macdonald R, Belkin HE, Wall F, Bagiński B (2009) Compositional variation in the chevkinite group: new data from igneous and metamorphic rocks. Mineral Mag 73:777–796

Macdonald R, Bagiński B, Kartashov PM, Zozulya D, Dzierżanowski P (2015a) Hydrothermal alteration of chevkinite-group minerals. Part 2. Metasomatite from the Keivy massif, Kola Peninsula. Russia. Mineral Mag 79:1039–1059

Macdonald R, Bagiński B, Kartashov PM, Zozulya D, Dzierżanowski P (2015b) Interaction of chevkinite-(Ce) with hydrothermal fluids; evidence from metasomatites of the Haldzan Buragtag massif, Mongolian Altai. Can Mineral 53:1015–1034. https://doi.org/10.3749/canmin.140002.3

Macdonald R, Bagiński B, Belkin HE, Stachowicz M (2019) Composition, paragenesis and alteration of the chevkinite group of minerals. Am Mineral 104:349–367

Monchoux P, Fontan F, de Parseval P, Martin RF, Wang RC (2006) Igneous albitite dikes in orogenic lherzolites, Western Pyrénées, France: a possible source for corundum and alkali feldspar xenocrysts in basaltic terranes. 1. Mineral Ass Can Mineral 44:817–842

Nagashima M, Armbruster T, Akasak M, Sano-Furukawa A, Nishio-Hamane D, Maisy A, Imaoka T, Nakashima K (2020) Multi-methodical study of the Ti, Fe^{2+} and Fe^{3+} distribution in chevkinite-subgroup minerals: X-ray diffraction, neutron diffraction, [57]Fe Mössbauer spectroscopy and electron-microprobe analyses. Phys Chem Mineral 47:29

Nejbert K, Bagiński B, Kotowski J, Jokubauskas P, Jurewicz E, Macdonald R (2020) Chevkinite-group minerals in Poland. Acta Geol Pol 70:97–106

Pouchou JL, Pichoir JF (1991) Quantitative analysis of homogeneous or stratified microvolumes applying the model 'PAP.' In: Heinrich KFJ, Newbury DE (eds) Electron Probe Quantification. Plenum Press, New York, 31–75

Prol-Ledemsa R-M, Melgarejo JC, Martin RF (2012) The El Muerto "NYF" granitic pegmatite, Oaxaca, Mexico, and its striking enrichment in allanite-(Ce) and monazite-(Ce). Can Mineral 50:1055–1076

Proshchenko YG (1967) Rare earth minerals from albitites of eastern Siberia. In: Mineralogiya pegmatitov i gidrotermalitov shchelochnykh massivov. Akademii Nauk SSSR, Institut Mineralogii, Geokhimii, Kristallokhimii Redk. Elementov, Moscow, 103–136. (in Russian)

Rämö OT, Haapala I (1995) One hundred years of rapakivi granite. Mineral Petrol 52:129–185

Rickwood PC (1989) Boundary lines within petrologic diagrams which use oxides of major and minor elements. Lithos 22(4):247–263

Ryka W (1982) Prekambryjska Ewolucja Platformy Wschodnioeuropejskiej. Geol Quart 26:257–272

Ryka W (1993) Crystalline basement of Suwalszczyzna (NE Poland). Przeg Geol 41:546–551 (in Polish)

Ryka W, Sawicki L (1980) Aktualny stan badań utworów prekambryjskich w Polsce i kierunki ich rozwoju. Kwart Geol 24(1):89–105

Seifert W, Kramer W (2003) Accessory titanite: an important carrier of zirconium in lamprophyres. Lithos 71:81–98

Shumlyanskyy L, Hawkesworth C, Billström K, Bogdanova S, Mytrokhyn O, Romer R, Dhuime B, Cleasson S, Ernst R, Whitehouse M, Bilan O (2017) The origin of the Palaeoproterozoic AMCG complexes in the Ukrainian shield: New U-Pb ages and Hf isotopes in zircon. Precamb Res 292:216–239

Skridlaite G, Wiszniewska J, Duchesne JC (2003) Ferro-potassic A-type granites and related rocks in NE Poland and S Lithuania: west of the East European Craton. Precamb Res 124:305–326

Spiridonov EM, Filimonov SV, Semikolennykh ES, Korotayeva NN, Krivitskaya NN (2019) Chevkinite-(Ce) and perrierite-(Ce) in the island arc quartz gabbro-norite-dolerites of the Ayu-Dag intrusion, Rocky Crimea. Proc Russ Mineral Soc 148 (4):61–79. (in Russian)

Stachowicz M, Bagiński B, Welch MD, Kartashov PM, Macdonald R, Balcerzak J, Tyczkowski J, Woźniak K (2019) Cation ordering, valence states, and symmetry breaking in the crystal-chemically complex mineral chevkinite-(Ce): X-ray diffraction and photoelectron spectroscopy studies and mechanisms of Nb enrichment. Am Mineral 104:595–602

Sun SS, McDonough WF (1989) Chemical and isotopic systematics of oceanic basalts: applications for mantle composition and processes. In: Saunders AD, Norry MJ (eds) Magmatism in the Ocean Basins. Geol Soc, London, Spec Publ 42:313–345

Sundblad K, Mansfeld J, Motuza G, Ahl M, Claesson S (1994) Geology, geochemistry and age of a Cu-Mo-bearing granite at Kabeliai, southern Lithuania. Mineral Petrol 5:43–57

Vlach SRF, Gualda GAR (2007) Allanite and chevkinite in A-type granites and syenites of the Graciosa Province, southern Brazil. Lithos 97(1–2):98–121

Vlach SRF, Gualda GAR, Steele IM, Vilalva FCJ (2014) Chevkinite → allanite reaction relationships in silicic rocks. Workshop on accessory minerals, 24–26 September, Warsaw. Book of Abstracts, 44–41

Vorma A (1976) On the petrochemistry of rapakivi granites with special reference to the Laitila massif, southwestern Finland. Geol Surv Finland Bull 285

Wiszniewska J, Kusiak MA, Krzemińska E, Dörr W, Suzuki K (2007) Mesoproterozoic AMCG granitoids in the Mazury Complex, NE Poland- a geochronological update. In: Kozłowski A, Wiszniewska J (eds) Granitoids in Poland. AM Monograph No 1. Komitet Nauk Mineralogicznych Polskiej Akademii Nauk-Wydział Geologii Uniwersytet Warszawski, 31–39

Wiszniewska J, Krzemińska E, Williams IS, Krzemiński L (2016) AMCG suite in NE Poland; subsequent datings of A-type granitoids on SHRIMP. 8th SHRIMP Workshop, 6–10 September 2016, Granada, Spain, 87–89

Wybraniec S (1999) Transformation and visualization of potential field data. Pol Geol Inst, Spec Pap 1:1–88

Zozulya D, Macdonald R, Bagiński B (2020) REE fractionation during crystallization and alteration of fergusonite-(Y) from Zr-REE-Nb–rich late- to post-magmatic products of the Keivy alkali granite complex, NW Russia. Ore Geol Rev 125:103693